Optics Communications 527 (2023) 128978

Contents lists available at ScienceDirect

Optics Communications

journal homepage: www.elsevier.com/locate/optcom

Noise-tolerant single-photon imaging by using non-diffractive pulsed laser beams

Huiyu Qi [a], Guangyue Shen [a,d], Zhaohui Li [a], Haotian Shi [a], Chao Hang [a,b,c,*], Guoxiang Huang [a,b,c], Guang Wu [a,c,d,*]

[a] State Key Laboratory of Precision Spectroscopy, East China Normal University, Shanghai 200062, China
[b] NYU-ECNU Institute of Physics, New York University at Shanghai, Shanghai 200062, China
[c] Collaborative Innovation Center of Extreme Optics, Shanxi University, Taiyuan, Shanxi 030006, China
[d] Chongqing Key Laboratory of Precision Optics, Chongqing Institute of East China Normal University, Chongqing 401120, China

ARTICLE INFO

Keywords:
Single-photon imaging
Noise-tolerance
Non-diffraction
Pulsed Bessel beam

ABSTRACT

Accurate optical imaging capable of reconstructing three-dimensional (3D) target objects with strong surrounding noises are highly demanding in diverse applications. For conventional imagers with narrow probe beams, the probe beams usually suffer from serious spreading and distortion due to the diffraction and surrounding noises. Here, we construct a 3D imager by using pulsed Bessel beams, enabling reconstruction of high-resolution 3D profiles with sub-millimeter transverse resolution and sub-centimeter depth resolution. We demonstrate that due to the outstanding diffraction-free and self-healing properties of Bessel beams, the present imager can provide high-quality reconstructed images in high-noise environments with opaque scatters. The method developed here for reducing the effects of surrounding noises can also be exploited in the light detection and ranging technology at single-photon level.

1. Introduction

Active three-dimensional (3D) optical imaging systems reconstruct 3D images for remote target objects by projecting probe laser beams onto the objects and detecting the back-scattered ones. In the last decades, the research of 3D imaging has attracted a lot of attentions due to its widespread applications in diverse fields, including machine-vision and ranging [1,2], terrestrial mapping [3], remote sensing [4], environmental monitoring [5,6], target recognition and identification [7], satellite-based global topography [8], and so on. An increasing demand for these applications has further promoted the development of 3D imaging, which are required to be able to reconstruct high-resolution 3D profiles not only over a long range but also with low illumination power. For this aim, latest single-photon detection techniques [9,10] have been used in imaging systems, which enables imaging over a long range with very low flux of backscattered photons [11–14]. Additionally, artificial intelligence assisted imaging [15,16] has also been suggested, which may have the potential of great improvement on imaging quality and range. Further, due to the recent advances in the integration of photonic and electronic circuits [17], a large-scale two-dimensional array of coherent detector pixels operating as a light detection and ranging (LiDAR) system can be served as a universal 3D imaging platform [18].

On the other hand, it is more challenging to realize high-resolution imaging in the presence of strong surrounding noises. In this direction, a full waveform LiDAR that can identify small echo peaks superimposed on the background envelope has been used to detect targets under adverse weather conditions [19]. Additionally, in order to temporally gate out unwanted back-reflections from noises, temporal window of 6 ns is used for a silicon single-photon avalanche photodiode (APD) detector with the time resolution less than 50 ps to improve the performance of 3D imaging in highly scattering underwater environments [20]. Moreover, based on the technique of quantum frequency up conversion, the time resolution is further improved to ~6 ps so that the 3D imaging of targets obscured by strongly scattering media can be realized [21,22]. For instance, in ref [21] the 3D profile of obscured scene is successfully reconstructed, where the target is located 2 mm behind an obscuring aluminum wire mesh. However, in most previous imaging schemes, Gaussian probe beams are usually adopted in the systems, which cannot recover their original waveforms after being obstructed by the scatters, leading to the low quality of reconstructed images.

In this work, we build up a 3D optical imaging system by using non-diffractive pulsed Bessel beams, which are not only immune to diffraction (and hence shape-preserving for a very narrow beam and a long propagation distance) but also self-healing (and hence highly

* Corresponding authors at: State Key Laboratory of Precision Spectroscopy, East China Normal University, Shanghai 200062, China.
E-mail addresses: chang@phy.ecnu.edu.cn (C. Hang), gwu@phy.ecnu.edu.cn (G. Wu).

https://doi.org/10.1016/j.optcom.2022.128978
Received 16 May 2022; Received in revised form 25 August 2022; Accepted 6 September 2022
Available online 12 September 2022

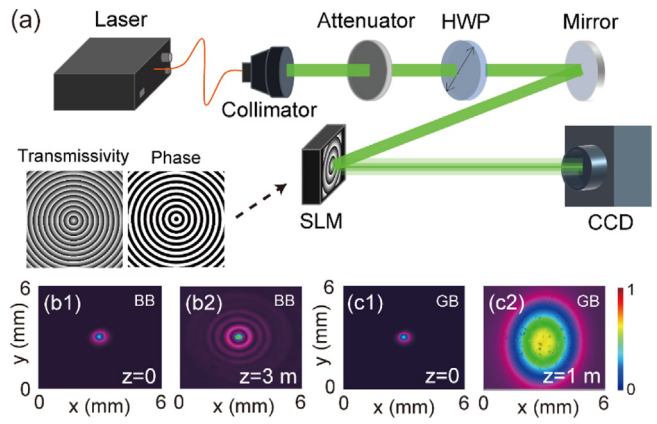

Fig. 1. High-quality Bessel Beams. (a) The experimental setup for generating high-quality long-range Bessel beams. Here, HWP, SLM, and CCD stand for half-wave plate, spatial light modulator, and charge-coupled device, respectively. The transmissivity and phase of the SLM are shown in the inset. (b1) and (b2) Intensity distributions of the Bessel beam measured by the CCD camera at $z = 0$ m and 3 m, respectively. (c1) and (c2) Intensity distributions of the Gaussian beam measured by the CCD camera at $z = 0$ m and 1 m, respectively. BB: Bessel beam; GB: Gaussian beam.

noise-tolerant) [23,24]. Particularly, we construct a 3D imager for a range over 3 meters by using pulsed Bessel beams, enabling reconstruction of high-resolution 3D profiles with 0.6 mm transverse resolution and 1 cm depth resolution, while the light energy per pulsed Bessel beam is lowered to about 20 nJ. We highlight that due to the outstanding diffraction-free and self-healing capabilities of Bessel beams the present imager can provide high-quality reconstructed images in high-noise environments, where conventional imagers are completely break down. The method developed in this work for suppressing the diffraction and conquering the noises in optical imaging pave the way for designing novel low-cost, diffraction-free, and noise-tolerant 3D imagers by using various non-diffractive beams such as high-order Bessel beams (Bessel vortexes), Gauss–Laguerre beams, and Airy beams [25–27].

2. High-quality Bessel beams

Before constructing a 3D imager by using the pulsed Bessel beams, we first develop high-quality Bessel beams over tens of meters (one order longer than the propagation distance obtained in [28]). In particular, we use a high-resolution liquid-crystal-on-silicon (LCOS) spatial light modulator (SLM), which can realize the functionality of a glass axicon. The pixel number of the LCOS SLM used in our experiment arrives 4094 × 2400 in the size of 3.74 × 3.74 μm square; the analogue base angle of the LCOS SLM can be estimated as

$$\theta_{analog} = \arctan\left(\lambda_p/d\right) \approx 1.26 \times 10^{-3}\text{Rad} \tag{1}$$

where the probe wavelength $\lambda_p = 532$ nm and the period of SLM phase along the radial direction $d \approx 4.2$ μm. We stress that compared with the smallest base angle that glass axicons can achieve, the analogue base angle of LCOS SLM, θ_{analog}, can be one order smaller, resulting in longer axial extent of Bessel beams, which is $\sim 1/\theta_{analog}$. Moreover, θ_{analog} can be precisely manipulated in situ through tuning the parameter d.

The experimental setup is illustrated in Fig. 1(a). A Gaussian beam at the wavelength of 532 nm is emitted from a solid state laser. The initial waist width of the Gaussian beam is 3.0 mm and it propagates through a collimator, an attenuator, and a half-wave plate in turns. Afterwards, the Gaussian beam is reflected by a LCOS SLM, where it is transformed into a zeroth-order Bessel beam with the radius of the central spot $w \approx 0.22$ mm. Finally, the Bessel beam is measured by a moving charge-coupled-device (CCD) camera along the propagation direction.

The SLM typically works with laser beams only in one particular polarization and incident angle. In the experiment, the polarization of the incident Gaussian beam is tuned to be perpendicular to the liquid crystal molecules of the SLM through a half-wave-plate. In addition, the angle between the incident Gaussian beam and the normal direction of the SLM is around 5 degrees. During the scanning process, the polarization and incident angle are fixed.

The intensity distributions of a Bessel (Gaussian) beam measured at $z = 3$ m ($z = 1$ m) is presented in Fig. 1(b2) [Fig. 1(c2)]. We find that the radius of the central spot of the Bessel beam is increased from 0.22 mm to 0.35 mm (about 1.6 times) over a total propagation distance of 3 m, however, the width of a Gaussian beam is increased from 0.22 mm to 2.6 mm (about 11.8 times) in the same propagation distance. In order to estimate the importance of diffraction, we exploit the Fresnel number, defined as $F = w^2/(L\lambda_p)$ with w the probe beam width and L the total propagation distance. In the present setup, we have a very small Fresnel number $F \approx 0.03$, indicating that a strong diffraction effect plays a role in the beam propagation [29]. In fact, the propagation distance of the Bessel beams generated in our experimental can be extended to more than 20 m. In this case, the Bessel beam displays nearly no distortion during its propagation up to $z = 10$ m, a manifestation of its excellent diffraction-free property. At $z = 20$ m, although the interference rings of the Bessel beam is exhausted completely, the center spot of the Bessel beam survives except that it suffers the diffraction-induced spreading and attenuation.

3. High-resolution 3D imaging based on pulsed Bessel beams

After obtaining the high-quality long-range Bessel beams, we proceed to develop the 3D imaging by using the pulsed Bessel beams. A pulsed Bessel beam has a localized temporal profile and the same diffraction-free and self-healing capabilities with those of a Bessel beam. If the temporal profile is localized and can be described by a Gaussian function, the probe field with the form of pulsed Bessel beams is written as

$$\vec{E}_p\left(\vec{r},t\right) = \vec{e}_x A_0 J_0\left(k_r,\vec{r}\right) e^{-\frac{(t-z/c)^2}{\tau^2}-\alpha^2 r^2} e^{i\left(k_z z-\omega_p t\right)} + c.c. \tag{2}$$

where $\vec{r} = (x, y)$ are transverse coordinates, $\vec{e}_x$ is the unit polarization vector of the probe field (assumed to be along the x direction), A_0 is the beam amplitude, k_r (k_z) is the wavenumber in the transversal directions (longitudinal direction), and τ is the temporal width of the pulse. Additionally, a small decay factor α ($0 < \alpha \ll 1$) is introduced to ensure the containment of the infinite Bessel function tail and makes the laser power normalizable. All values of parameters A_0, k_r, and α can be determined from the experimental measurements.

The energy of each pulsed Bessel beam can be obtained by the energy flux integrated over the pulse duration, i.e. $E_{pulse} = \sqrt{\pi}\epsilon_0 c A_0^2 \tau \int_0^\infty r^2 dr J_0(k_r, r)^2 e^{-2\alpha^2 r^2}$. In the experiment, we have $k_r \approx 1.2 \times 10^4$ m-1, $\tau \approx 1$ ns, and $\alpha \approx 0.05$, which leads to the energy per pulse $E_{pulse} \approx 20$ nJ. Such a low energy is due to the fact that the central spot of the zeroth-order Bessel beam can be focused in a very small cross-sectional area and it is invariant during the propagation as the beam is non-diffractive.

Shown in Fig. 2(a) is the setup of a 3D imager by using the pulsed Bessel beams. Here, a nanosecond pulse laser is served as the light source for illumination. The pulsed Gaussian beam emitted from the light source is transformed into a pulsed Bessel beam after propagating through a collimator, an attenuator, and a half-wave plate in turns, and is reflected over a LCOS SLM the same with that used in Fig. 1(a). After scattered by the target objects, the back-propagating probe pulses propagate through a lens and a bandpass filter. Eventually, they are received by a silicon single-photon avalanche photodiode (Si SPAD) with each signal pulse contains only 0.14 photon in average (see Appendix A for more details). Note that the energy per pulse after scattering is much lower than E_{pulse}, i.e. most of energy of the pulsed Bessel beams is lost during the scattering process. The emission and reception events are time stamped by a time-to-digital converter (TDC)

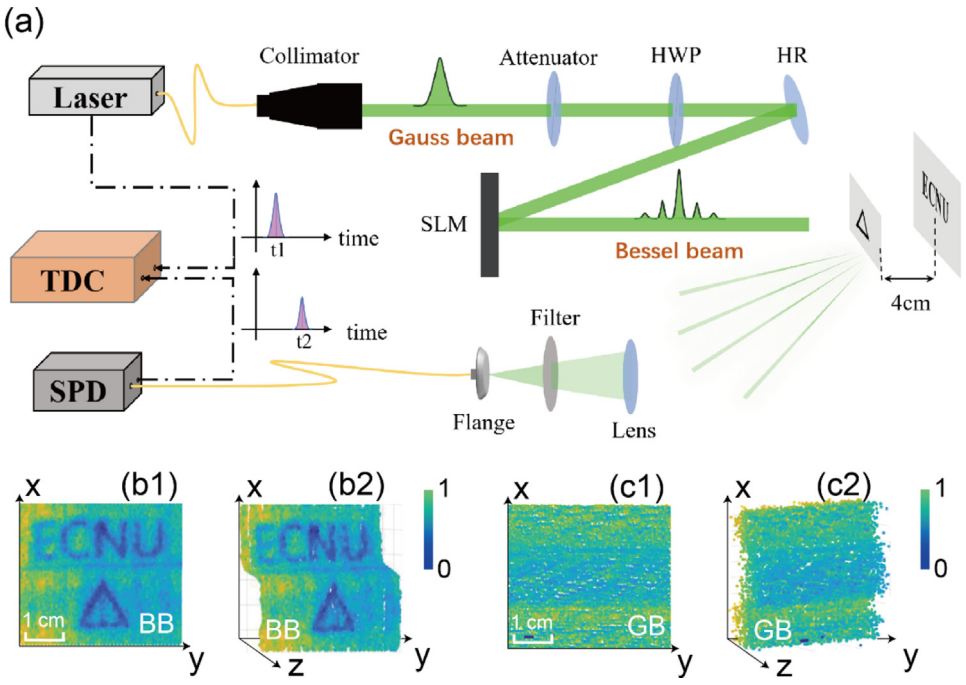

Fig. 2. High-resolution 3D imaging based on pulsed Bessel beams. (a) The experimental setup of a diffraction free and noise-tolerant 3D imager by using the pulsed Bessel beams. Here, SPD and TDC stand for single-photon detector and time-to-digital converter, respectively. (b1)–(b2) [(c1)–(c2)] The front and side views of target objects by using the pulsed Bessel (Gaussian) beams.

to measure the time of flight (ToF) of photons with the time resolution of 64 ps. However, the timing resolution of the whole system needs a full consideration including not only the timing resolution of the TDC but also the timing resolution of the Si-APD, the timing jitter of the laser, and so on. Thus, the timing resolution of the whole system is usually much longer than 64 ps. Moreover, since the background noise may be strong enough to cover the probe signals, we isolate the signals from noises by further using the time–frequency matched filtering [30]. Particularly, the time–frequency matched filter correlates, in time and frequency domains, a time–frequency distribution (TFD) of the received signal with the TFD of the known signal. Thus, it is very useful to detect a known signal embedded in a strong background noise and has many important applications including radar and sonar systems. Finally, with the data of time delay between the emission and reception for each pulsed Bessel beam, it is possible to reconstruct the target object in 3D.

In the experiment, the imaging rang of the imager is set to be 3 m. The target objects include a small metal plate carved with a regular triangle Δ and a large metal plate carved with letters "ECNU". The side length of the regular triangle Δ is only 10 mm; the width, height, and weight of each letter is 7 mm, 5 mm, and 1 mm, respectively. The separation between the two metal plates is 4 cm along the z direction.

Fig. 2(b1)–(b2) [(c1)–(c2)] show the reconstructed 3D images of target objects by using the pulsed Bessel (Gaussian) beams. We implement raster scanning by installing the whole imaging system on a high-speed motorized stage. Thereby, the imaging system can rotate in both horizontal and longitudinal directions in a well-controlled way. During the scanning, the imager is rotated 133 times in the horizontal direction (from left to the right) and then it is rotated 1 time in the longitudinal direction (from top to bottom). In addition, each rotation is followed by a stop lasting about 0.3 s for collecting and processing date. After 87 cycles, i.e. 133*87 times of rotations, the detections cover the whole target objects and a complete 3D image can be reconstructed. For obtaining high-quality reconstructed 3D images, we repeat the detections for each pixel (each image contains 133*87=11571 pixels) by 10 thousand times and average the signals to improve the timing resolution (reduce the time jitter) of the system. Meanwhile, we carefully measure the time of flight (ToF) difference of the pulse intensity peaks. By doing so, the timing resolution of the imager can be lowered to about 0.1 ns, corresponding to the depth resolution of 3 cm (below the separation between the front and behind target objects). Since the transverse spreading of the center spot of the Bessel beam is less than 0.08 mm for the 3-meter-long propagation distance, the smallest distinguishable size of the target objects in the transversal direction can be less than 0.6 mm. We also expect that sub-centimeter depth resolution is achievable with higher timing resolution of the system and shorter pulses in the present imager.

The temporal invariance of the pulsed Bessel beams is important for our imager. Fig. 3(a) shows the temporal width of the pulsed Bessel beams as a function of the imaging range z, where the experimental (numerical) results are indicated by the samples (lines). It is clear that the increase of the ration between the temporal width and its initial value (τ/τ_0) is less than 10% within the imaging range of 3 m. The intensity peak of the pulsed Bessel beams is also traced and found to be invariant. Thus, the temporal profile of the pulsed Bessel beams is indeed temporally invariant during the propagation.

The quality of reconstructed images can be characterized by the imaging correlation J, defined as

$$\mathrm{J}(z) = \iint_S dxdyB(x,y,z)B(x,y,0) \Big/ \left[\iint_S dxdyB(x,y,z) \iint_S dxdyB(x,y,0)\right] \tag{3}$$

where S denotes the area of reconstructed images and B denotes the brightness of objects in reconstructed images. From the above definition, it is easily seen that $\mathrm{J} = 1$ at $z = 0$ and $0 < \mathrm{J} < 1$ for $z > 0$.

Fig. 3(b) and (c) show respectively the imaging correlation J as a function of the imaging range z for the pulsed Bessel and Gaussian beams, where the experimental (numerical) results are indicated by the samples (lines). The simulation results are in a good agreement with the experimental results. We see that when the imaging range is increased from 0 to 3 m, the imaging correlation J by using the pulsed Bessel (gaussian) beam is decreased slowly (rapidly) from 1 to 0.65 (nearly 0). Thus, the quality of reconstructed images by using the pulsed Bessel beams is much better than that by using the pulsed Gaussian beams.

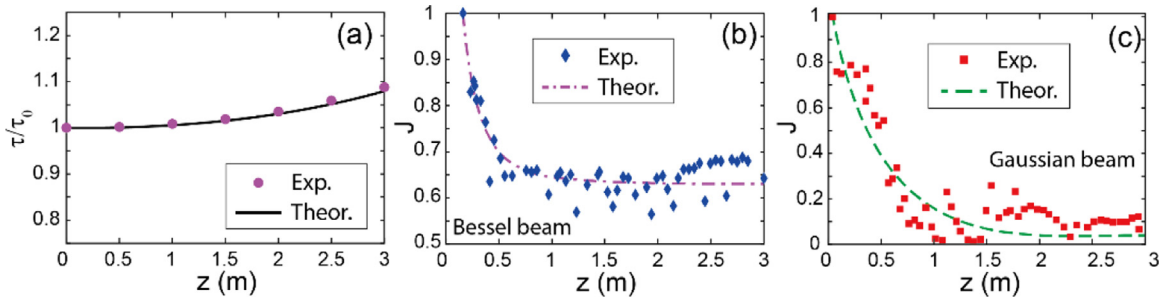

Fig. 3. (a) The ratio pulse duration of the pulsed Bessel beams as a function of the imaging range z; (b) [(c)] The imaging correlation J as a function of the imaging range z for the pulsed Bessel (Gaussian) beams. Both experimental (blue diamonds and red squares) and numerical (purple dash-dotted and green dashed lines) results are presented and agree with each other. BB: Bessel beam; GB: Gaussian beam.

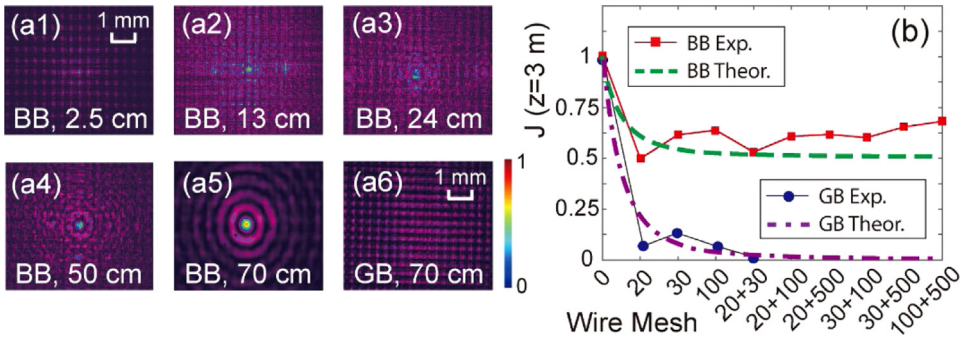

Fig. 4. Self-healing of a pulsed Bessel beam after it propagating through an aluminum wire mesh. (a1)–(a5) The self-healing of the pulsed Bessel beam just passing through a single aluminum wire mesh with the mesh hole number 20. The intensity distributions of the Bessel beam are illustrated at 2.5 cm, 13 cm, 24 cm, 50 cm, and 70 cm behind the wire mesh; (a6) The intensity distribution of a pulsed Gaussian beam at z = 70 cm behind the same wire mesh. BB: Bessel beam; GB: Gaussian beam. (b) The imaging correlation J as a function of the hole number for a single aluminum wire mesh or two wire meshes for the imaging range of 3 m. Both experimental (blue circles and red squares) and numerical (purple dash-dotted and green dashed lines) results are presented and have a good agreement.

4. Noise tolerance of the Bessel-beam-assisted 3D imaging

As the last step, we turn to the self-healing property of the pulsed Bessel beams and demonstrate that our imager is highly noise-tolerant and can work in a high-noise environment. To this end, we first show the self-healing phenomenon of a pulsed Bessel beam after it propagating through an aluminum wire mesh. Fig. 4(a1)–(a5) illustrates the intensity distributions of a pulsed Bessel beam at different distances behind the wire mesh, captured by the CCD camera. It is seen that the pulsed Bessel beam can reconstruct its initial intensity distribution at 70 cm behind the wire mesh. As a comparison, Fig. 4(a6) illustrates the intensity distribution of a pulsed Gaussian beam at 70 cm behind the same wire mesh. Since the lack of the self-healing property, the pulsed Gaussian beam suffers complete distortion.

Fig. 4(b) shows the imaging correlation J as a function of the mesh hole number of a single aluminum wire mesh or two aluminum wire meshes (for further increasing the strength of noises) for the imaging range of 3 m. It is seen that J drops slightly (rapidly) when the hole number is increased by using the pulsed Bessel (Gaussian) beams. Particularly, in the case of using pulsed Bessel beams, J saturates at around 60% when the hole number reaches a critical value, corresponding to rather strong noises. In this figure, both experimental (samples) and numerical (lines) results are presented and have a good agreement.

Next we carry out the same image reconstruction (i.e. the same pulsed Bessel beams and the imaging rang) by placing an aluminum wire mesh, served as opaque scatters, between the LCOS SLM and the target objects [see Fig. 5(a)]. The highly reflective mesh reduces the backscattered photons from the target objects while inducing backscattering ahead of the desired target. The left-top and right-bottom insets of Fig. 5(a) show respectively photographs of the target objects without and with the aluminum wire mesh through the direct telescope observation. The target objects are almost completely obscured by a combination of 100- and 500-hole wire meshes. Fig. 5(b1) and (b2) show the front and side views of the target objects by using the Bessel-beam-assisted imager. It is seen that the target objects can be clearly observed by the imager although they are completely obscured by the wire mesh in the direct telescope observation. In order to enhance the randomness of the backscattering, we have also used different combinations of wire meshes and place the wire meshes at different locations between the LCOS SLM and the target objects. We find that the target objects can still be clearly observed by the imager.

We have also carried out experiment by replacing the aluminum wire mesh with an air bubble film, served as non-opaque scatters. The results are shown in Fig. 5(c1) and (c2). In contrast with the wire mesh, the air bubble film poses a great challenge to the self-healing mechanism as one part of the laser beam can interfere with other parts, leading to interference-induced distortion in the reconstructed images. From the results, we find that the Bessel-beam-assisted 3D imaging can operate not only with opaque obscurants but also with non-opaque ones, highlighting their applications in extremely complex environments.

5. Conclusion

In conclusion, we have built up a 3D optical imaging system by using non-diffractive pulsed beams. We have shown that the present imager can work in high-noise environments with opaque scatters. The method developed here for reducing the effects of diffraction and surrounding noises paves the way for designing low-cost, diffraction-free, and noise-tolerant 3D imagers by using various non-diffractive pulsed beams at single-photon level, and can be used in LiDAR systems.

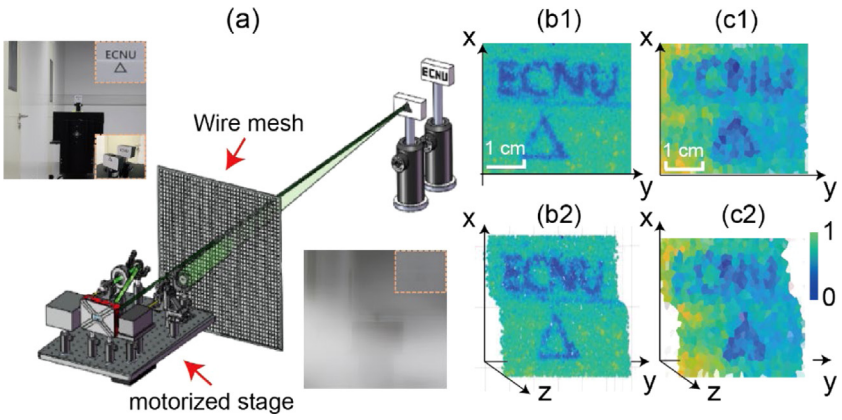

Fig. 5. Noise tolerance of the Bessel-beam-assisted 3D imaging. (a) The experimental setup. The imager is installed on a motorized stage; an aluminum wire mesh is placed between the LCOS SLM and the target objects. Left-top and right-bottom insets show respectively photographs of the target objects without and with the aluminum wire mesh through the direct telescope observation. (b1) and (b2) [(c1) and (c2)] Front and side views of the reconstructed image of the target objects by placing an aluminum wire mesh (air bubble film) between the LCOS SLM and the target objects, respectively.

Declaration of competing interest

The authors declare that they have no known competing financial interests or personal relationships that could have appeared to influence the work reported in this paper.

Data availability

Data will be made available on request.

Funding

National Natural Science Foundation of China (11804099, 11621404, 11974117, 11975098); National Key Research and Development Project of China (2017YFA0304201); Shanghai Municipal Science and Technology Major Project, China (No. 2019SHZDZX01).

Appendix A. Experimental setup

In our experiment, the laser system emits laser beams with the wavelength of 532 nm and the pulse duration of 1 ns, working at the pulse repetition frequency of 127 kHz. The high-quality Bessel beam is generated by a liquid crystal-on-silicon reflective spatial light modulator (HD SLM4KR, UPOLabs, China) with a high resolution of 4094×2400 pixels in the size of 15.311×8.976 mm. The filter (FL532-10, Thorlabs, US) allows the laser beams passing through with the central wavelength 532 ± 2 nm and the transmissivity 70%@532 nm. The back-scattered signals are received by a single-photon avalanche diode (SPCM-AQRH-16-FC, Excelitas Technologies, US) with the detection efficiency 50%@532 nm. The time delay between two laser beams scattered from the closer and farther target objects is monitored by a time-to-digital converter (Hydra Harp 400, Pico-Quant, Germany) with the timing resolution down to 64 ps.

Here, we use a silicon single-photon avalanche photodiode (Si SPAD) operating in the Geiger mode for counting the number of photons. In the period of 0.3 s, the SPAD captures 1254 photon from each pixel of the reconstructed image. Bearing in mind that the detection efficiency of the SPAD is about 50%, there are actually 2508 photons reaching the SPAD. On the other hand, since the pulse repetition frequency of the laser source is 127 kHz, 38100 pulses are generated in the period of 0.3 s. Consequently, there are $2508/38100 \approx 0.066$ photons containing in each pulse of Bessel beams. Finally, taking into account that the transmissivity of the filter is about 70% and the fiber-optic coupling efficiency is about 67%, the average number of photons per pulse is about two times of 0.066, which is about 0.14.

In addition, we have used a single aluminum wire mesh and a combination of two wire meshes with different hole numbers to simulate the surrounding noises with different strengths. The specification of wire meshes is given as

Wire Mesh 20: The hole size is 0.970×0.970 mm2, the wire diameter is 0.23 mm;

Wire Mesh 30: The hole size is 0.546×0.546 mm2, the wire diameter is 0.20 mm;

Wire Mesh 100: The hole size is 0.154×0.154 mm2, the wire diameter is 0.10 mm;

Wire Mesh 500: The hole size is 0.038×0.038 mm2, the wire diameter is 0.015 mm.

Appendix B. Theoretical treatment

The envelope of the probe field $E_p(x, y, z)$ can be described by the Maxwell equation under the paraxial approximation

$$i2k_p \frac{\partial E_p}{\partial z} + \left(\frac{\partial^2}{\partial x^2} + \frac{\partial^2}{\partial y^2} \right) E_p + V\left(\vec{r}\right) E_p = 0 \tag{B.1}$$

where the position vector $\vec{r} = (x, y, z)$ and the potential $V\left(\vec{r}\right) = V_{SLM}\left(\vec{r}\right) + V_{noise}(\vec{r})$. Here $V_{SLM}\left(\vec{r}\right)$ is a complex potential describing the action of the high-resolution liquid-crystal-on-silicon (LCOS) spatial light modulator (SLM) and $V_{noise}(\vec{r})$ is a complex potential describing the effect of surrounding noises. The real and imaginary parts of $V_{SLM}\left(\vec{r}\right)$ and $V_{noise}(\vec{r})$ stand for the phase shift and absorption of the probe beam resulted from the LCOS SLM and the surrounding noises, respectively.

The generation and propagation of Bessel beams can be performed in the following two-step process. In the first step, the incident probe beam with a Gaussian intensity distribution propagates with the potential $V_{SLM}\left(\vec{r}\right)$ while $V_{noise}\left(\vec{r}\right) = 0$. Due to the action of $V_{SLM}\left(\vec{r}\right)$, the Gaussian input beam will be transformed into a Bessel beam. In the second step, the Bessel beam propagates with the potential $V_{noise}\left(\vec{r}\right)$ while $V_{SLM}\left(\vec{r}\right) = 0$. In this step, the Bessel beam propagates from the LCOS SLM to the target objects in the presence of surrounding noises.

For the convenience of following discussion, Eq. (B.1) can be further written into a non-dimension form

$$i\frac{\partial u}{\partial \zeta} + \frac{d}{2}\left(\frac{\partial^2}{\partial \xi^2} + \frac{\partial^2}{\partial \eta^2} \right) u + V(\xi, \eta, \zeta)\, u = 0 \tag{B.2}$$

where new variables are defined as $\zeta = z/z_0$, $d = z_0/L_{diff}$, $(\xi, \eta) = (x, y)/w$, and $u = E_p/A_0$. Here z_0, L_{diff}, w, and A_0 are respectively the typical propagation distance, the characteristic diffraction length, the typical beam radius, and the typical amplitude of the probe beam; the

characteristic diffraction length is defined as $L_{diff} = 2\pi w^2/\lambda_p$ and the non-dimension potential is given by $V(\xi,\eta,\zeta) = z_0 V(\vec{r})/(2k_p)$. We can also write Eq. (B.2) into the form

$$\frac{\partial u}{\partial \zeta} = \hat{D}u + iV(\xi,\eta,\zeta)u \tag{B.3}$$

where $\hat{D} = i\frac{d}{2}\left(\frac{\partial^2}{\partial\xi^2} + \frac{\partial^2}{\partial\eta^2}\right)$ is the diffraction operator. Since Eq. (B.3) is a linear one, it can be solved analytically.

Now setting $V(\xi,\eta,\zeta) = V_{SLM}(\xi,\eta)$ for $0 < \zeta < \alpha$ and $V(\xi,\eta,\zeta) = V_{noise}(\xi,\eta)$ for $\alpha < \zeta < \beta$, where α is an effective length measuring the action of the LCOS SLM and β is the separation between the LCOS SLM and target objects, Eq. (B.3) can be further splitted into a set of equations:

$$\frac{\partial u}{\partial \zeta} = iV_{SLM}(\xi,\eta)u \tag{B.4}$$

for the first step ($0 < \zeta < \alpha$) and

$$\frac{\partial u}{\partial \zeta} = \hat{D}u + iV_{noise}(\xi,\eta)u \tag{B.5}$$

for the second step ($\alpha < \zeta < \beta$). Consequently, Eq. (B.4) gives the solution $u(\xi,\eta,\zeta = \alpha) = u(\xi,\eta,\zeta = 0)e^{iV_{SLM}(\xi,\eta)\alpha}$, where the initial condition $u(\xi,\eta,\zeta = 0)$ is chosen as a Gaussian function. Due to the action of the potential $V_{SLM}(\xi,\eta)$, $u(\xi,\eta,\zeta = \alpha)$ can acquire the form of the zeroth-order Bessel function. Eq. (B.5) gives the solution

$$u(\xi,\eta,\zeta = \beta) = F_T^{-1}\left\{\int_\alpha^\beta d\zeta F_T\left[\hat{D} + iV_{noise}(\xi,\eta)u(\xi,\eta,\zeta = \alpha)\right]\right\} \tag{B.6}$$

where F_T denotes the Fourier-transform operation from the spatial domain to the momentum domain. Due to the diffraction-free and self-healing properties of Bessel beams, the probe beam will preserve its waveform during the propagation in the presence of surrounding noises for a long distance.

References

[1] Y. Altmann, et al., Quantum-inspired computational imaging, Science 361 (2018) eaat2298.
[2] R. Tobin, et al., Three-dimensional single-photon imaging through obscurants, Opt. Express 27 (2019) 4590–4611.
[3] B. Schwarz, Mapping the world in 3D, Nat. Photon. 4 (2010) 429–430.
[4] J.C. Brock, et al., The emerging role of lidar remote sensing in coastal research and resource management, J. Coast. Res. 53 (2009) 1–5.
[5] A. Konishi, et al., 3D lidar imaging for detecting and understanding plant responses and canopy structure, J. Exp. Bot. 58 (2006) 881–898.
[6] G. Zhao, et al., Mobile lidar system for environmental monitoring, Appl. Opt. 56 (2017) 1506–1516.
[7] A.B. Gschwendtner, et al., Development of coherent laser radar at Lincoln laboratory, Linc. Lab. J. 12 (2000) 383–396.
[8] D. Smith, et al., Topography of the northern hemisphere of Mars from the Mars orbiter laser altimeter, Science 279 (1998) 1686–1692.
[9] D. Faccio, et al., A trillion frames per second: The techniques and applications of light-in-flight photography, Rep. Progr. Phys. 81 (2018) 105901.
[10] D. Shin, et al., Photon-efficient imaging with a single photon camera, Nature Commun. 7 (2016) 12046.
[11] A.M. Pawlikowska, A. Halimi, R.A. Lamb, G.S. Buller, Single-photon three-dimensional imaging at up to 10 kilometers range, Opt. Express 25 (2017) 11919–11931.
[12] Z.-P. Li, et al., Single-photon computational 3D imaging at 45 km, Photon. Res. 8 (2020) 532.
[13] Z.-P. Li, et al., Super-resolution single-photon imaging at 8.2 kilometers, Opt. Express 28 (2020) 4076–4087.
[14] Z.-P. Li, et al., Single-photon imaging over 200 km, Optica 8 (2021) 344.
[15] Z. Niu, et al., Photon-limited face image super-resolution based on deep learning, Opt. Express 26 (2018) 22773C22782.
[16] D. Feng, et al., Deep active learning for efficient training of a LiDAR 3D object detector, 2019, p. 10609, arXiv preprint arXiv:1901.
[17] I. Kim, et al., Nanophotonics for light detection and ranging technology, Nature Nanotechnol. 16 (2021) 508–524.
[18] C. Rogers, et al., A universal 3D imaging sensor on a silicon photonics platform, Nature 590 (2021) 256–261.
[19] A.M. Wallace, et al., Full waveform LiDAR for adverse weather conditions, IEEE Trans. Veh. Technol. 69 (7) (2020) 7064.
[20] A. Maccarone, et al., Underwater depth imaging using time-correlated single-photon counting, Opt. Express 23 (2015) 33911.
[21] P. Rehain, et al., Noise-tolerant single photon sensitive three-dimensional imager, Nature Commun. 11 (2020) 921.
[22] S. Maruca, et al., Non-invasive single photon imaging through strongly scattering media, Opt. Express 29 (2021) 9981.
[23] J. Durnin, et al., Diffraction free beams, Phys. Rev. Lett. 58 (1987) 1499.
[24] D. McGloin, et al., Bessel beams: Diffraction in a new light, Contemp. Phys. 46 (2005) 15.
[25] J. Arlt, et al., Generation of high-order bessel beams by use of an axicon, Opt. Commun. 177 (2000) 297C301.
[26] G.A. Siviloglou, et al., Observation of accelerating airy beams, Phys. Rev. Lett. 99 (2007) 213901.
[27] A. Chong, et al., Airy-Bessel wave packets as versatile linear light bullets, Nature Photon. 4 (2010) 103–106.
[28] C. Vetter, et al., Realization of free space long-distance self-healing Bessel beams, Laser Photon. Rev. 13 (2019) 1900103.
[29] The Fresnel number F in previous works usually lies in the range $0.1 < F < 1$, corresponding to a smaller dispersion than that in the present work. This is because in the previous works wide Gaussian laser pulses with near-infrared wavelength are frequently used.
[30] F. Hlawatsch, et al., Time-frequency projection filters and time-frequency signal expansions, IEEE Trans. Signal Process. 42 (1994) 3321C3334.